ACS OMEGA

http://pubs.acs.org/journal/acsodf

Article

Aluminum Oxide Nanoparticle Films Deposited from a Nonthermal Plasma: Synthesis, Characterization, and Crystallization

Zhaohan Li, Parker R. Wray, Magel P. Su, Qiaomiao Tu, Himashi P. Andaraarachchi, Yong Jin Jeong, Harry A. Atwater, and Uwe R. Kortshagen*

Cite This: *ACS Omega* 2020, 5, 24754−24761

Read Online

ACCESS | Metrics & More | Article Recommendations | Supporting Information

ABSTRACT: Aluminum oxide, both in amorphous and crystalline forms, is a widely used inorganic ceramic material because of its chemical and structural properties. In this work, we synthesized amorphous aluminum oxide nanoparticles using a capacitively coupled nonthermal plasma utilizing trimethylaluminum and oxygen as precursors and studied their crystallization and phase transformation behavior through postsynthetic annealing. The use of two reactor geometries resulted in amorphous aluminum oxide nanoparticles with similar compositions but different sizes. Size tuning of these nanoparticles was achieved by varying the reactor pressure to produce amorphous aluminum oxide nanoparticles ranging from 6 to 22 nm. During postsynthetic annealing, powder samples of amorphous nanoparticles began to crystallize at 800 °C, forming crystalline θ and γ phase alumina. Their phase transformation behavior was found to be size-dependent in that powders of small 6 nm amorphous particles transformed to form phase-pure α-Al_2O_3 at 1100 °C, while powders of large 11 nm particles remained in the θ and γ phases. This phenomenon is attributed to the fast rate of densification and neck formation in small amorphous aluminum oxide particles.

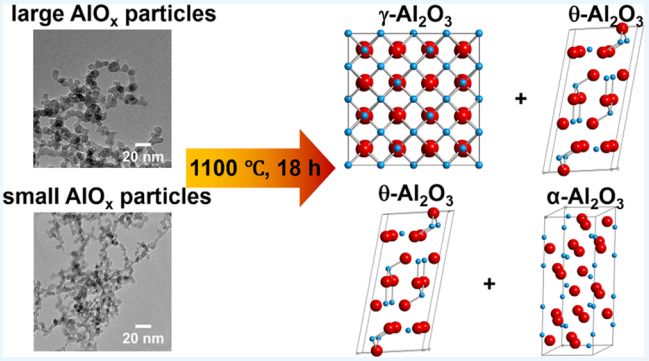

1. INTRODUCTION

Aluminum oxide (Al_2O_3), commonly known as alumina, is one of the most widely used inorganic ceramic materials because of its superior thermal, chemical, and structural properties. Alumina can exist in both amorphous and crystalline forms. Amorphous alumina is considered to be an excellent candidate for anodic materials, gate insulators in transistors, protective coatings, and catalysts.[1−5] Various methods have been employed to synthesize amorphous alumina nanoparticles, which include sol−gel processing,[6,7] solution combustion,[8−12] precipitation,[13−15] ultrasonic treatment of porous anodic alumina membranes,[16] energetic pulsed laser ablation,[17] and tragacanth gel synthesis.[18]

The structure of amorphous alumina has been studied extensively and found to be comprised of a network of AlO_4 tetrahedra, AlO_5 polyhedra, and small fractions of AlO_6 octahedra.[19−24] Solid-state ^{27}Al nuclear magnetic resonance studies revealed that the existence of a significant fraction of AlO_5 polyhedra, where Al^{3+} ions are penta-coordinated with oxygen ions, creates disorder and hinders the crystallization and growth of crystalline alumina phases.[25] Thus, high temperatures (~800 °C) are required for the transformation of amorphous to crystalline alumina nanoparticles.[26] This process involves a structural rearrangement reaction converting AlO_5 polyhedra into AlO_4 and AlO_6.

Phase transformation of amorphous to crystalline alumina nanoparticles can greatly depend on several parameters such as the synthetic route, heating rate, grain size, and chemical composition. Crystalline alumina can exist in various metastable crystalline phases (χ, η, δ, κ, θ, γ, and ρ)[27−29] and corundum, or α-alumina is identified as the most thermodynamically stable phase in bulk form. The typical phase transformation sequence in crystalline alumina can be depicted as $\gamma \rightarrow \delta \rightarrow \theta \rightarrow \alpha$-$Al_2O_3$.[26] The transformation of γ-Al_2O_3 (density ρ = 3.56 g cm^{-3}) to α-Al_2O_3 (ρ = 3.98 g cm^{-3}) is accompanied by a volume reduction of about 10% and proceeds through a meta-phase of θ-Al_2O_3.[30] Typically, the final transformation to α-Al_2O_3 requires higher annealing temperature around 1100 °C.[26] With superior hardness, low friction, unique heat-transfer properties, and excellent wear resistance, α-Al_2O_3 plays a critical role in the production of advanced ceramic materials and as a core and filler material for nanocomposites.[31−33] γ-Al_2O_3 nanoparticles themselves also

Received: July 13, 2020
Accepted: August 31, 2020
Published: September 14, 2020

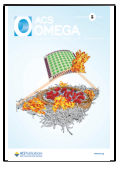

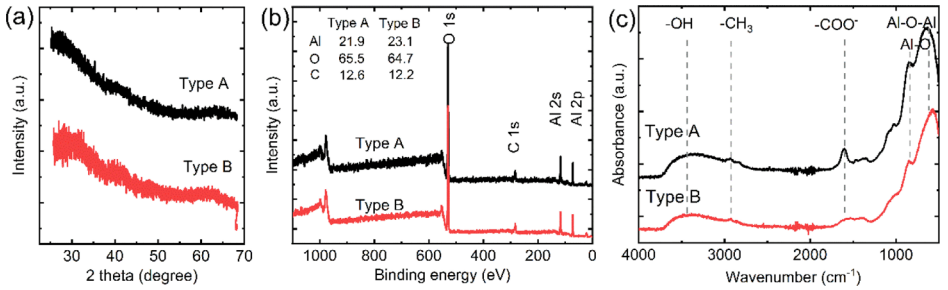

Figure 1. Characterization of AlO_x nanoparticles synthesized from type A and type B reactors at p = 3.8 Torr: (a) θ–2θ mode out-of-plane XRD patterns of the as-synthesized AlO_x nanoparticles from type A and type B reactors. (b) XPS survey scan of AlO_x nanoparticles from type A and type B reactors. (c) Typical FTIR spectra of AlO_x samples from type A and type B reactors, with major absorption peaks featuring Al–O, $-COO^-$, $-CH_3$, and −OH.

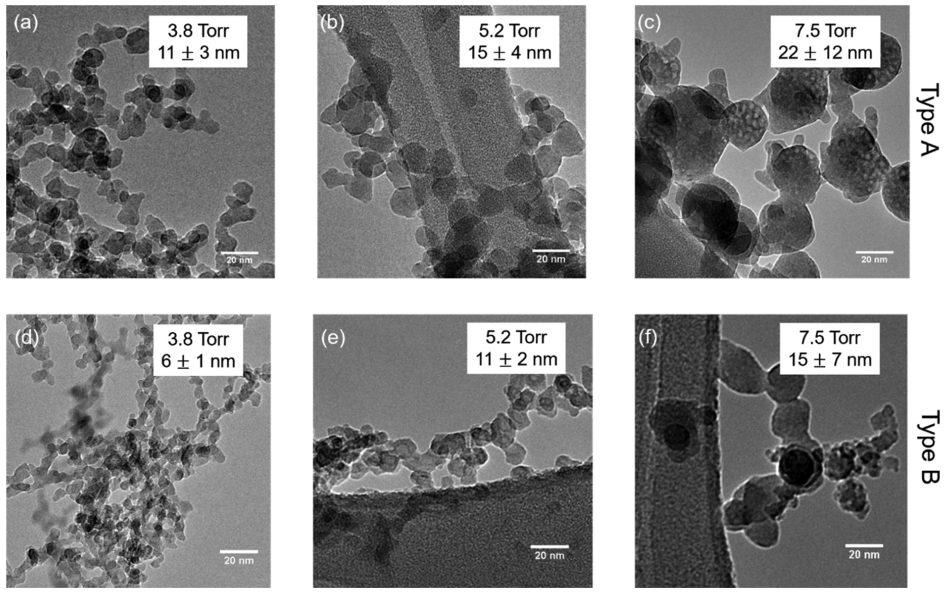

Figure 2. TEM images of AlO_x nanoparticles synthesized from type A (a–c) and type B (d–f) reactors at pressures of 3.8, 5.2, and 7.5 Torr with mean sizes and standard deviations.

exhibit excellent catalytic properties because of their surface acidity and high surface area.[34]

In this work, we synthesized amorphous alumina nanoparticles by a nonthermal plasma approach and studied their crystallization and phase transformation behavior during postsynthetic annealing. Nonthermal plasma synthesis has shown the potential to produce a variety of nanoparticles with high purity and narrow size distributions, and the library of nanoparticle materials has been expanded from group-IV semiconductors to metal oxides and metal sulfides.[35−41] Furthermore, nanoparticles made by this method can be directly deposited into particle films with densities ranging from 20 to 60%.[42,43] The as-deposited aluminum oxide nanoparticles are annealed at 600−1100 °C for the investigation of their phase transformation behavior.

2. RESULTS AND DISCUSSION

2.1. Synthesis of Amorphous Alumina Nanoparticles.

Amorphous alumina (AlO_x) nanoparticles were synthesized using the two reactor geometries shown in the experimental section. Figure 1a shows the X-ray diffraction (XRD) spectra of as-synthesized AlO_x nanoparticle samples from both type A and B reactors at p = 3.8 Torr. The absence of definitive peaks in XRD suggests that the as-synthesized AlO_x nanoparticles are amorphous. As shown in a previous study, amorphous alumina nanoparticles have the lowest surface energy and are more thermodynamically stable compared to θ- and α-phase polymorphs at small particle sizes.[46]

X-ray photoelectron spectroscopy (XPS) and Fourier-transform infrared spectroscopy (FTIR) measurements were performed to evaluate the surface and atomic composition of AlO_x nanoparticles from both reactor configurations (Figure 1b,c). For both samples, the main peaks in XPS correspond to O 1s, C 1s, and Al 2p at 530, 284, and 73 eV, respectively, confirming the elemental composition of AlO_x nanoparticles. Carbon incorporation (5−10 at %) is commonly observed when trimethylaluminum (TMA) is used as the aluminum source because of strong Al−C bonds.[47−49] The carbon content can be partly due to contamination in air, as samples are shortly exposed to air during the transfer, but can also originate from the methyl groups in TMA. Atomic percentage ratios of Al to O are around 1:3 for both A and B type reactor samples, with carbon percentages around 10−15%. The atomic ratios are in general not affected by the plasma power used for synthesis (Figure S1). High-resolution XPS spectra were analyzed to gain insight into the composition of both types of AlO_x nanoparticle samples (Figure S2). The binding energy of the Al 2p peak at ∼74.6 eV corresponds to Al−O bonding in

https://dx.doi.org/10.1021/acsomega.0c03353
ACS Omega 2020, 5, 24754−24761

alumina.[50,51] The O 1s peak at ~531.5 eV can be resolved into two individual peaks representing O^{2-} and OH^{-}.[51−53] FTIR spectra for samples from both reactor types reveal absorption bands related to hydroxyl (−OH), alkyl (C−H), (C−O), and aluminum species (Al−O and Al−O−Al). The peak around ~670 cm^{-1} and the shoulder located around ~860 cm^{-1} correspond to the Al−O stretching vibrations in five-fold coordinated AlO_5 and four-fold coordinated AlO_4, respectively. Features from AlO_6 stretching vibrations could also be present, which according to the literature lie in the 400−650 cm^{-1} spectral range and overlap with Al−O stretching vibrations and oscillations in AlO_4 and AlO_5.[47,54,55]

Statistics of AlO_x nanoparticle size was determined using transmission electron microscopy (TEM). At p = 3.8 Torr, the average size of AlO_x nanoparticles from type A and type B reactors is 11 ± 3 and 6 ± 1 nm, respectively. The different particle sizes can be explained by the different plasma densities at the point of TMA injection. Nanoparticle growth in plasmas proceeds through the nucleation of clusters, many of which are initially neutral.[56] These clusters quickly coagulate to form nanoparticles, leading to a reduction of the overall concentration of clusters and particles. When the cluster/nanoparticle density has dropped to the level of the ion density in the plasma, there are sufficient electrons to charge most particles negatively and suppress further coagulation.[56] In the type B reactor, the TMA precursor is injected into a higher density plasma zone compared to the type A reactor, where the precursor is injected into a less dense plasma afterglow. Coagulation in the type B reactor is therefore suppressed at smaller particle sizes, corresponding to higher particle concentrations, compared to the type A reactor. For each type of reactor, size tuning of AlO_x nanoparticles can be achieved by varying the reactor pressure. This changes the particle residence time in the plasma and therefore tunes the time of surface growth. TEM images of as-synthesized AlO_x nanoparticles from type A and B reactors under three sets of reactor pressures are shown in Figure 2. At each pressure, the type B reactor produces smaller particles than the type A reactor. For both reactor configurations, the mean particle size increases with increasing pressure. At 3.8 and 5.2 Torr, AlO_x nanoparticles from both reactors are aggregated but nearly spherical in shape and have relatively narrow size distributions (Figure S3). At the relatively high pressure of 7.5 Torr, AlO_x nanoparticles exhibit a bimodal size distribution with both small and large irregular nanoparticles present.

We estimated the process yield of each type of reactor setup by measuring the weight of the AlO_x nanoparticle powders collected at p = 3.8 Torr for 10 min. With a fixed substrate position, samples collected from both types of reactor setups were piles of white powders (Figure S4). The sample weights from the type A and B reactors were 3.2 and 7.0 mg, respectively. This corresponds to yields of 19.2 and 42.0 mg h^{-1}. The current production rates are limited by the TMA and oxygen flow rates because of safety considerations.

We deposited AlO_x nanoparticle films by rastering a substrate beneath the reactor output orifice to study the optical properties of AlO_x nanoparticle films. The films were deposited with 240 raster passes and examined by scanning electron microscopy (SEM) and Mueller matrix measurements. The thicknesses of the AlO_x nanoparticle films were measured to be 7.1 ± 1.1 and 9.1 ± 0.9 μm for type A and type B reactors, respectively. Characteristic cross-sectional SEM images of the nanoparticle films are shown in Figure 3.

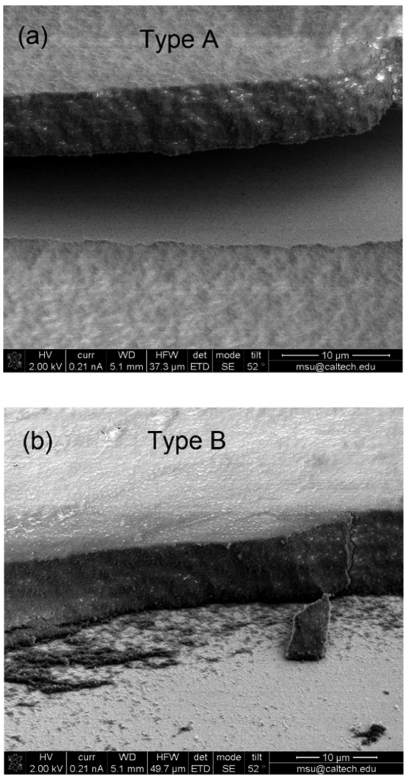

Figure 3. Cross-sectional SEM images of AlO_x nanoparticle laminate films synthesized from type A (a) and type B reactors (b). A correction factor of 1/cos(38°) is applied in the y-axis to account for the tilt of the setup with respect to the SEM Everhart−Thornley detector.

Mueller matrix measurements, which allow for the characterization of anisotropic-depolarizing samples, including cross-polarization, were performed to extract the effective (homogenized) complex permittivity of the particle films. The measurements were also used to determine the complex permittivity of the corresponding AlO_x nanoparticles. In both type A and B films, no polarization conversion from p-polarized to s-polarized or vice versa was present. The Mueller matrix data showed only noise for elements mm_{13}, mm_{31}, mm_{22}, mm_{23}, mm_{32}, mm_{41}, and mm_{42}. Furthermore, mm_{12} = mm_{21}. This block diagonal structure of the Mueller matrix indicates that the type A and B samples can be treated as macroscopically isotropic.[57−59] Therefore, the effective permittivity of each sample can be represented by a wavelength-dependent scalar. The nanoparticle films were best homogenized using the Bruggeman mixing formula. This formula has been shown to consistently produce an effective permittivity that accurately models nanoparticle films, including anisotropic-depolarizing effects.[60−65] Maxwell−Garnett and linear mixing formulas were also explored, but they less accurately modeled the measured data. The permittivity of the individual nanoparticles was modeled using Gaussian oscillators to represent amorphous phonon resonances while satisfying the Kramers−Kronig relations. For the type A film, a sample thickness of 7.75 μm and a particle fill fraction of 22.3% provided the best fit to the optical interference patterns in a nearly lossless region of the amorphous alumina film between 4000 and 6250 cm^{-1}. For the type B film, a thickness of 9.23 μm and a fill fraction of 19.4% provided the best fit. Further details about Bruggeman homogenization and the correspond-

https://dx.doi.org/10.1021/acsomega.0c03353
ACS Omega 2020, 5, 24754−24761

ing Gaussian oscillator model, including tables for the oscillator parameters, can be found in the Supporting Information. Figure 4 shows the reconstructed imaginary part of the particle

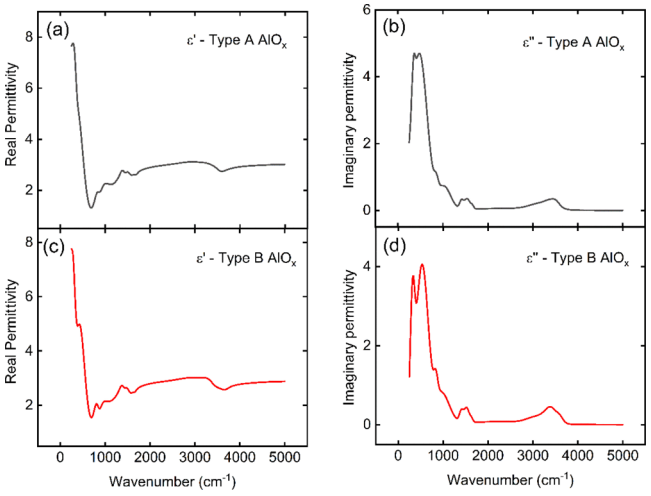

Figure 4. Real and imaginary parts of the complex AlO_x nanoparticle films' permittivity found in the type A reactor (a,b) and type B reactor (c,d), respectively.

permittivity. Strong oscillators in the 300−700 cm^{-1} spectral range correspond to AlO_4, AlO_5, and AlO_6 stretching vibrational modes. These values corroborate our results from FTIR as well as the literature.[47,54,55,63] Similar to our findings from XPS and FTIR, the reconstructed permittivity shows that the particles from both types of reactors have a similar chemical composition. The depolarization constant for type A and B reactor films was 0.261 ± 0.005 and 0.407 ± 0.006, respectively. This indicates predominant scattering of sphere-like inclusions post deposition. All of the above characterizations reveal that particles from type A and type B reactors have similar compositions but different sizes.

2.2. Crystallization Behavior of Powder Samples of Amorphous Alumina Nanoparticles. In a nonthermal plasma, crystallization of nanoparticles can occur through the heat generated by the recombination of electrons and ions on the nanoparticle surfaces.[66,67] Here the as-produced AlO_x nanoparticles have amorphous structures, indicating that particle heating from the nonthermal plasma is not sufficient to induce crystallization. Postsynthetic annealing of powder samples of amorphous alumina nanoparticles was explored to induce their crystallization and subsequent phase transformation to networks of crystalline alumina nanoparticles.

To study the crystallization and phase transformation behavior of powder samples of amorphous AlO_x nanoparticles, a pile of AlO_x nanoparticles was collected and annealed in a Thermo Scientific Lindberg Blue furnace at temperatures ranging from 400 to 1100 °C in the atmosphere. Samples collected in this manner are expected to have porosities >80% and consist of loose agglomerates of nanoparticles.[42] Some of the agglomerates may have already been formed in the gas phase before deposition. The temperature ramp rate was ∼50 °C min^{-1}. Since the properties of powder samples of small AlO_x nanoparticles are of primary interest, we explored the crystallization behavior of samples synthesized at 3.8 Torr from type A and B reactors. Phase transformation of amorphous alumina typically proceeds through the amorphous-to-γ and γ-to-α phase transitions[68,69] or with an additional transition to the θ-phase between the transformation from the γ- to α-phase,[70] before reaching the thermodynamically stable α-phase. Our observations reveal that powder samples of AlO_x nanoparticles from both types of reactors begin to crystallize at 800 °C producing a mixture of θ- and γ-phases, as shown in Figure 5a,b. The crystallization temperature is consistent with that from the literature.[9,46]

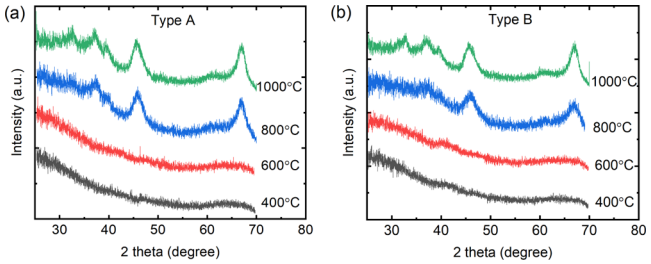

Figure 5. XRD patterns of the postsynthesis annealed AlO_x nanoparticles from (a) type A and (b) type B reactors, with annealing temperatures ranging from 400 to 1000 °C and an annealing time of 18 h.

As the annealing temperature increased up to 1100 °C, we observed that the powder samples of AlO_x nanoparticles from the type A and B reactors form different crystalline phases (Figure 6). The samples of larger AlO_x nanoparticles from the

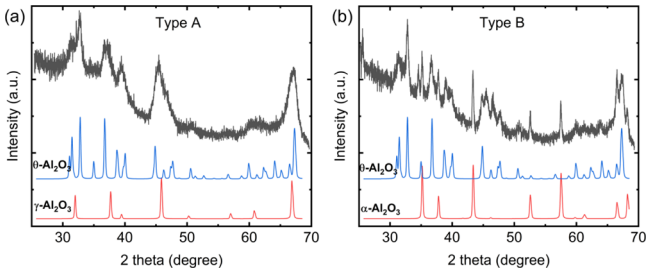

Figure 6. XRD patterns of the postheated AlO_x nanoparticles from (a) type A and (b) type B. Both samples were annealed at 1100 °C for 18 h. The bottom columns in both graphs show the reference profiles of γ-, θ-, and α-phase aluminum oxides.

type A reactor form a mixture of θ- and γ-phases at 1100 °C, whereas the samples of smaller AlO_x nanoparticles from the type B reactor form a mixture of θ- and α-phases. Time of postsynthetic annealing also affects phase transformation of the type B reactor AlO_x nanoparticle powders. When the annealing time increased up to 40 h, type B AlO_x nanoparticle powders form particle networks of phase pure α-Al_2O_3 nanocrystals (Figure 7).

This transformation is also accompanied by a significant crystal growth. The mean crystallite sizes of crystalline alumina particles after 18 h annealing were estimated using Scherrer fittings. Annealing for 18 h of ∼6 nm AlO_x nanoparticle powders at 1100 °C resulted in a particle network consisting of a mixture of ∼30 nm θ-Al_2O_3 and >100 nm α-Al_2O_3 particles (Figure S5). Samples of phase-pure α-Al_2O_3 particles obtained after 40 h are also estimated to be comprised of nanocrystals larger than 100 nm. The crystalline grain sizes are confirmed by TEM images (Figure 7b,c). It is interesting to observe that the powders of larger AlO_x nanoparticles from the type A reactor never exhibit α-Al_2O_3 phase even with longer annealing times.

https://dx.doi.org/10.1021/acsomega.0c03353
ACS Omega 2020, 5, 24754−24761

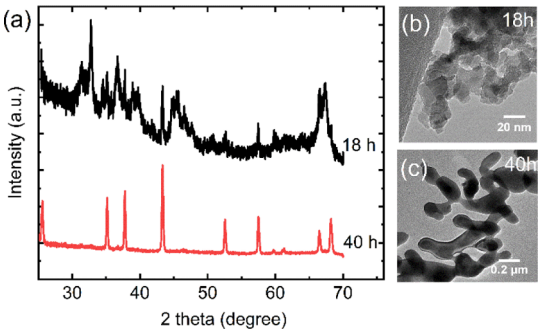

Figure 7. (a) XRD pattern of type B AlO_x nanoparticles heated at 1100 °C for 18 and 40 h; TEM images of (b) AlO_x nanoparticles annealed at 1100 °C for 18 h and (c) AlO_x nanoparticles annealed at 1100 °C for 40 h.

As the powder samples of AlO_x nanoparticles from both types of reactors have a similar composition, we postulated that the difference in their phase transformation behavior is likely due to the different sizes of their as-synthesized constituent particles. To test this assumption, we investigated the phase transformation behavior of powder samples of the large AlO_x particles with mean sizes around 11 and 15 nm synthesized in the type B reactor with higher reactor pressures. XRD patterns taken after 18 h of annealing time reveal that powders of smaller ∼6 nm AlO_x nanoparticles form α-phase Al_2O_3 along with θ-Al_2O_3, while powders of larger ∼11 and ∼15 nm AlO_x nanoparticles only form θ-Al_2O_3 and do not exhibit any α-phase features (Figure S6). These observations support our assumption that powders of initially smaller size AlO_x nanoparticles have a higher tendency to transform to the α-phase after annealing.

It has been pointed out that necking and densification of particles start to occur when annealing amorphous AlO_x nanoparticles, forming nanoporous structures before crystallization.[46,71,72] It is likely that during the annealing, the rate of densification and neck formation is faster in powder samples of smaller particles compared to larger particles as the neck growth is dominated by mass transport and is thus enhanced in smaller size particles.[73] The fact that powder densification can be promoted by a decrease of particle sizes has also been observed in other nanoparticle systems.[74] After neck growth, the interconnected structures tend to transform to α-phase Al_2O_3 as the temperature further increases because it is the thermodynamically stable phase for bulk Al_2O_3.

3. CONCLUSIONS

Amorphous alumina nanoparticles with average sizes ranging from 6 to 22 nm were successfully synthesized using a nonthermal plasma approach with two different reactor geometries with typical yields of 19 and 42 mg h^{-1}, respectively. Infrared Mueller matrix measurements indicated that the optical properties of the nanoparticle film could be modeled by a homogenized effective refractive index. The homogenized refractive index of the particle film was shown to be accurately represented using the Bruggeman effective medium model. Based on this model, particle fill fractions were estimated to be around 20% for both type A and type B reactors. Furthermore, the refractive index of the amorphous alumina nanoparticles was modeled using Gaussian oscillators, showing clear AlO_4, AlO_5, AlO_6, and Al−OH spectral peaks, matching reports in the literature. Post-thermal annealing of powder samples of AlO_x particles from both types of reactors led to crystallization, forming a mixture of θ- and γ-phases at 800 °C, while powder samples of small AlO_x nanoparticles with average diameters of ∼6 nm were transformed into phase-pure α-Al_2O_3 upon annealing at 1100 °C. Powder samples of larger AlO_x nanoparticles never formed α-Al_2O_3.

4. EXPERIMENTAL SECTION

4.1. Nanoparticle Synthesis. For the synthesis of amorphous alumina (AlO_x) nanoparticles via nonthermal plasma, TMA and oxygen (O_2) gas were used as precursors, with argon as the carrier gas. In the plasma region, TMA is decomposed via electron impact or radical abstraction reactions, forming reactive metal atoms or partially decomposed TMA fragments. The reactive species can subsequently react with oxygen atoms to form Al_2O_3.[44] We considered the following chemical equation to control appropriate flow rates

$$2Al(CH_3)_3 + 12O_2 \rightarrow Al_2O_3 + 6CO_2 + 9H_2O$$

Based on the stoichiometric molar ratio of TMA and oxygen (TMA/O_2 = 1:6), over 6 times more oxygen than TMA should be fed for complete oxidation of TMA to Al_2O_3 and other reaction products (CO_2 and H_2O). We chose an excess oxygen flow rate of 6 standard cubic centimeters per minute (sccm) compared with a TMA flow rate of 0.2 sccm.

A schematic of the two types of reactors used in this work is shown in Figure 8. AlO_x nanoparticles were synthesized in a

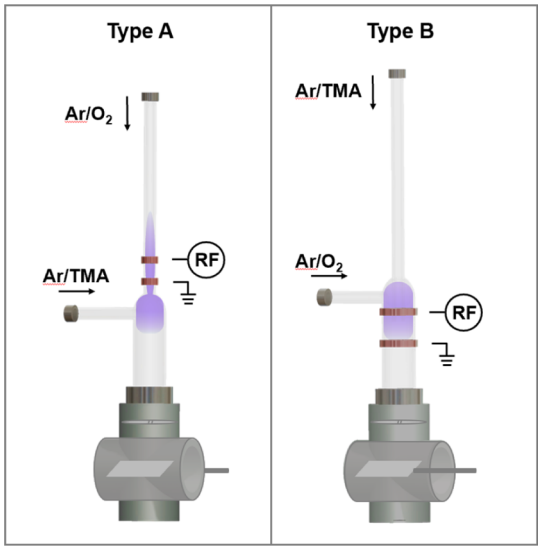

Figure 8. Schematic of the two types of nonthermal plasma reactors used for AlO_x nanoparticle synthesis and film deposition.

nonthermal, low pressure, flow-through reactor equipped with a 13.56 MHz radio frequency (RF) capacitively coupled plasma source similar to that used in refs 37 and 38. Because two precursors can spontaneously react with each other to produce uncontrolled products,[45] we injected both precursor species separately into the plasma for dissociation to occur in the plasma zone. There are two strategies that have been demonstrated before for the successful synthesis of metal oxide nanoparticles.[37,38] In the first method, denoted as type A, O_2 diluted in Ar gas was injected from the top inlet of the reactor and flowed through the region where RF power was applied. Meanwhile, 0.2 sccm of TMA vapor with 6 sccm of Ar gas was

https://dx.doi.org/10.1021/acsomega.0c03353
ACS Omega 2020, 5, 24754−24761

injected from a sidearm tube into the downstream region of the Ar/O_2 plasma. In this afterglow zone, AlO_x nanoparticles nucleated and grew. In the second method, denoted as type B, the TMA vapor diluted in Ar was injected through an inlet tube that extended into the main reactor chamber, while O_2 gas diluted with Ar gas was passed through a sidearm tube and into the space around the upper injection tube. The ring electrodes were placed such that the plasma initiated about 1 cm above the end of the top injection tube and the discharge extended downstream of the tube end in order to dissociate TMA and O_2 precursors individually before they mix in the main reactor chamber. The as-synthesized AlO_x nanoparticles in both configurations were collected on silicon wafers through a slit-shaped orifice where supersonic nanoparticle impaction produced a curtain of nanoparticles traveling at high speeds.[42] For each type of reactor, three pressure conditions were studied by using three different orifice sizes (0.3, 0.4, 0.5 mm × 8 mm) while keeping the gas flow rates constant.

For optical characterization, nanoparticle films were deposited by using the 0.5 mm × 8 mm orifice and passing a piece of Si wafer carrying a 300 nm Au film below the orifice with 240 raster passes. The gas flow rates and upstream and downstream pressures are summarized in Table 1.

Table 1. Summary of Synthesis Parameters Used in This Study

	gas	flow rate [sccm]	P_{up} [Torr]	P_{down} [Torr]
type A	O_2 diluted in Ar (O_2/Ar)	6(O_2)/60(Ar)	3.8	0.42
	TMA vapor with Ar (TMA/Ar)	0.2(TMA)/6(Ar)		
type B	O_2 diluted in Ar (O_2/Ar)	6(O_2)/60(Ar)	3.8	0.47
	TMA vapor with Ar (TMA/Ar)	0.2(TMA)/6(Ar)		

4.2. Characterization. XRD was performed with a Bruker D8 Discover 2D X-ray diffractometer equipped with a Co Kα radiation point source. Instrument broadening was obtained by measuring a standard LaB_6 crystal powder sample with the same scanning parameters (Figure S7). For XRD analysis, aluminum oxide nanoparticles were directly deposited onto Si wafers to form a pile of powder. The XRD patterns were converted to the wavelength of a Cu source (λ = 1.54 Å) for data analysis.

TEM images were taken from a Tecnai T12 microscope with an accelerating voltage of 120 kV. Nanoparticles were either directly deposited from the gas phase or drop-cast in a methanol dispersion on holey carbon TEM grids for imaging.

FTIR was performed with a Bruker ALPHA FTIR spectrometer using the attenuated total reflection (ATR) module in a nitrogen-filled glovebox. AlO_x nanoparticles were dispersed in methanol and drop-cast onto the ATR crystal. Nanoparticles were allowed to dry before taking measurements.

XPS was performed with a PHI Versa Probe III XPS and UPS system. For XPS analysis, aluminum oxide nanoparticles were deposited onto Si wafers with 30 raster passes to form a film.

Nanoparticle laminate film thicknesses were measured empirically by cross-sectioning the nanoparticle laminate films with a Ga focused ion beam and imaging with a scanning electron microscope (FEI Nova 600 NanoLab DualBeam) at a 52° tilt. The cross-sectioning was performed in two steps: a regular cross-section (30 kV, 1 nA) approximately 2 μm in width was cut first followed by a cleaning cross-section (30 kV, 30 pA). The thickness of the cross-sections was measured with ImageJ with a correction factor of 1/cos(38°) in the y-axis to account for the tilt.

To analyze the film optical properties, the first four columns of the angle- and wavelength-resolved Mueller matrix were measured in the reflection mode. Mueller matrix measurements were performed using an IR-VASE Mark II ellipsometer with an AutoRetarder from the J.A. Woollam Company. The configuration was polarizer−sample−compensator−analyzer. The measurement spectral range extended from 250 to 5000 cm^{-1} with a resolution of 7.7 cm^{-1}. The angular range was 40 to 70° from the surface normal, with an angular resolution of 5°. Data was averaged over 400 measurements—5 days of continuous measurement per sample under ambient conditions. Once the samples were measured, an oscillator model of the film permittivity was constructed using the software WVASE32 from J.A. Woollam. Model parameters such as the film thickness and particle fill fraction were initialized based on the empirical measurement averages and constrained by 3 times the measurement standard deviations. Initial values for the particle oscillator model were taken from the literature. All model parameters were simultaneously fitted using the full angle and wavelength-resolved Mueller matrix data.

■ ASSOCIATED CONTENT

Supporting Information

The Supporting Information is available free of charge at https://pubs.acs.org/doi/10.1021/acsomega.0c03353.

Atomic concentration in samples from type B reactor obtained by XPS with power varying from 5 W to 40 W; XPS high resolution spectra of Al 2p peak, O 1s peak, and C 1s peak; size distributions corresponding to the TEM images; photograph showing AlOx nanoparticles deposited from type A and type B reactors for same period of time; Scherrer fittings of XRD patterns; XRD patterns of samples from type B reactor for three nanoparticle sizes; and Gaussian oscillator parameters used to reconstruct the permittivity of nanoparticles from type A and type B reactors (PDF)

■ AUTHOR INFORMATION

Corresponding Author

Uwe R. Kortshagen − *Department of Mechanical Engineering, University of Minnesota, Minneapolis, Minnesota 55455, United States;* orcid.org/0000-0001-5944-3656; Email: kortshagen@umn.edu

Authors

Zhaohan Li − *Department of Mechanical Engineering, University of Minnesota, Minneapolis, Minnesota 55455, United States;* orcid.org/0000-0002-8155-7243

Parker R. Wray − *Thomas J. Watson Laboratories of Applied Physics, California Institute of Technology, Pasadena, California 91125, United States;* orcid.org/0000-0003-3384-0826

Magel P. Su − *Thomas J. Watson Laboratories of Applied Physics, California Institute of Technology, Pasadena, California 91125, United States;* orcid.org/0000-0003-4898-5024

https://dx.doi.org/10.1021/acsomega.0c03353
ACS Omega 2020, 5, 24754−24761

Qiaomiao Tu − *Department of Mechanical Engineering, University of Minnesota, Minneapolis, Minnesota 55455, United States;* orcid.org/0000-0001-7478-8687
Himashi P. Andaraarachchi − *Department of Mechanical Engineering, University of Minnesota, Minneapolis, Minnesota 55455, United States;* orcid.org/0000-0001-9736-1088
Yong Jin Jeong − *Department of Mechanical Engineering, University of Minnesota, Minneapolis, Minnesota 55455, United States;* orcid.org/0000-0003-4479-7683
Harry A. Atwater − *Thomas J. Watson Laboratories of Applied Physics, California Institute of Technology, Pasadena, California 91125, United States;* orcid.org/0000-0001-9435-0201

Complete contact information is available at: https://pubs.acs.org/10.1021/acsomega.0c03353

Notes

The authors declare no competing financial interest.

■ ACKNOWLEDGMENTS

This work is supported by the Army Research Office under MURI project under W911NF-18-1-0240. Parts of this work were carried out in the Characterization Facility, University of Minnesota, which receives partial support from the National Science Foundation through the MRSEC program grant DMR-1420013.

■ REFERENCES

(1) Boisier, G.; Raciulete, M.; Samélor, D.; Pébère, N.; Gleizes, A. N.; Vahlas, C. Electrochemical behavior of chemical vapor deposited protective aluminum oxide coatings on Ti6242 titanium alloy. *Electrochem. Solid-State Lett.* **2008**, *11*, C55−C57.
(2) Samélor, D.; Lazar, A.-M.; Aufray, M.; Tendero, C.; Lacroix, L.; Béguin, J.-D.; Caussat, B.; Vergnes, H.; Alexis, J.; Poquillon, D.; et al. Amorphous alumina coatings: processing, structure and remarkable barrier properties. *J. Nanosci. Nanotechnol.* **2011**, *11*, 8387−8391.
(3) Avis, C.; Jang, J. High-performance solution processed oxide TFT with aluminum oxide gate dielectric fabricated by a sol−gel method. *J. Mater. Chem.* **2011**, *21*, 10649−10652.
(4) Amini, G.; Najafpour, G. D.; Rabiee, S. M.; Ghoreyshi, A. A. Synthesis and Characterization of Amorphous Nano-Alumina Powders with High Surface Area for Biodiesel Production. *Chem. Eng. Technol.* **2013**, *36*, 1708−1712.
(5) Kang, D.; Tong, S.; Yu, X.; Ge, M. Template-free synthesis of 3D hierarchical amorphous aluminum oxide microspheres with broccoli-like structure and their application in fluoride removal. *RSC Adv.* **2015**, *5*, 19159−19165.
(6) Li, J.; Pan, Y.; Xiang, C.; Ge, Q.; Guo, J. Low temperature synthesis of ultrafine α-Al_2O_3 powder by a simple aqueous sol−gel process. *Ceram. Int.* **2006**, *32*, 587−591.
(7) Karim, M. R.; Rahman, M.; Miah, M.; Ahmad, H.; Yanagisawa, M.; Ito, M. Synthesis of γ-alumina particles and surface characterization. *Open Colloid Sci. J.* **2011**, *4*, 32−36.
(8) Laishram, K.; Mann, R.; Malhan, N. A novel microwave combustion approach for single step synthesis of α-Al_2O_3 nanopowders. *Ceram. Int.* **2012**, *38*, 1703−1706.
(9) Sathyaseelan, B.; Baskaran, I.; Sivakumar, K. Phase transition behavior of nanocrystalline Al_2O_3 powders. *Soft Nanosci. Lett.* **2013**, *03*, 69.
(10) Ozuna, O.; Hirata, G. A.; McKittrick, J. Pressure influenced combustion synthesis of γ- and α- Al_2O_3 nanocrystalline powders. *J. Phys.: Condens. Matter* **2004**, *16*, 2585.
(11) Toniolo, J. C.; Lima, M. D.; Takimi, A. S.; Bergmann, C. P. Synthesis of alumina powders by the glycine−nitrate combustion process. *Mater. Res. Bull.* **2005**, *40*, 561−571.
(12) Sharma, A.; Modi, O.; Gupta, G. K. Effect of fuel to oxidizer ratio on synthesis of Alumina powder using Solution Combustion Technique-Aluminium Nitrate & Glycine combination. *Adv. Appl. Sci. Res.* **2012**, *3*, 2151−2158.
(13) Su, X.; Chen, S.; Zhou, Z. Synthesis and characterization of monodisperse porous α- Al_2O_3 nanoparticles. *Appl. Surf. Sci.* **2012**, *258*, 5712−5715.
(14) Sanamyan, T.; Pavlacka, R.; Gilde, G.; Dubinskii, M. Spectroscopic properties of Er^{3+} doped α-Al_2O_3. *Opt. Mater.* **2013**, *35*, 821−826.
(15) Wang, J.; Ge, L.; Li, Z.; Li, L.; Guo, Q.; Li, J. Facile size-controlled synthesis of well-dispersed spherical amorphous alumina nanoparticles via homogeneous precipitation. *Ceram. Int.* **2016**, *42*, 8545−8551.
(16) Zhang, W. J.; Wu, X. L.; Fan, J. Y.; Huang, G. S.; Qiu, T.; Chu, P. K. Luminescent amorphous alumina nanoparticles in toluene solution. *J. Phys.: Condens. Matter* **2006**, *18*, 9937.
(17) Pan, C.; Shen, P.; Chen, S.-Y. Condensation, crystallization and coalescence of amorphous Al_2O_3 nanoparticles. *J. Cryst. Growth* **2007**, *299*, 393−398.
(18) Atrak, K.; Ramazani, A.; Taghavi Fardood, S. Green synthesis of amorphous and gamma aluminum oxide nanoparticles by tragacanth gel and comparison of their photocatalytic activity for the degradation of organic dyes. *J. Mater. Sci.: Mater. Electron.* **2018**, *29*, 8347−8353.
(19) Kunath-Fandrei, G.; Bastow, T. J.; Hall, J. S.; Jaeger, C.; Smith, M. E. Quantification of aluminum coordinations in amorphous aluminas by combined central and satellite transition magic angle spinning NMR spectroscopy. *J. Phys. Chem.* **1995**, *99*, 15138−15141.
(20) Lamparter, P.; Kniep, R. Structure of amorphous Al_2O_3. *Phys. B* **1997**, *234−236*, 405−406.
(21) Gutierrez, G.; Johansson, B. Molecular dynamics study of structural properties of amorphous Al_2O_3. *Phys. Rev. B: Condens. Matter Mater. Phys.* **2002**, *65*, 104202.
(22) Snijders, P. C.; Jeurgens, L. P. H.; Sloof, W. G. Structural ordering of ultra-thin, amorphous aluminium-oxide films. *Surf. Sci.* **2005**, *589*, 98−105.
(23) Lee, S. K.; Lee, S. B.; Park, S. Y.; Yi, Y. S.; Ahn, C. W. Structure of amorphous aluminum oxide. *Phys. Rev. Lett.* **2009**, *103*, 095501.
(24) Lizárraga, R.; Holmström, E.; Parker, S. C.; Arrouvel, C. Structural characterization of amorphous alumina and its polymorphs from first-principles XPS and NMR calculations. *Phys. Rev. B: Condens. Matter Mater. Phys.* **2011**, *83*, 094201.
(25) John, C. S.; Alma, N. C. M.; Hays, G. R. Characterization of transitional alumina by solid-statemagic angle spinning aluminium NMR. *Appl. Catal.* **1983**, *6*, 341−346.
(26) Levin, I.; Brandon, D. Metastable alumina polymorphs: crystal structures and transition sequences. *J. Am. Ceram. Soc.* **1998**, *81*, 1995−2012.
(27) Stumpf, H. C.; Russell, A. S.; Newsome, J.; Tucker, C. Thermal Transformations of Aluminas and Alumina Hydrates-Reaction with 44% Technical Acid. *Ind. Eng. Chem.* **1950**, *42*, 1398−1403.
(28) Lippens, B. C.; De Boer, J. H. Study of phase transformations during calcination of aluminum hydroxides by selected area electron diffraction. *Acta Crystallogr.* **1964**, *17*, 1312−1321.
(29) Morrissey, K. J.; Czanderna, K. K.; Carter, C. B.; Merrill, R. P. Growth of α-Al_2O_3 Within a Transition Alumina Matrix. *J. Am. Ceram. Soc.* **1984**, *67*, c88−c90.
(30) Lamouri, S.; Hamidouche, M.; Bouaouadja, N.; Belhouchet, H.; Garnier, V.; Fantozzi, G.; Trelkat, J. F. Control of the γ-alumina to α-alumina phase transformation for an optimized alumina densification. *Bol. Soc. Esp. Ceram. Vidrio* **2017**, *56*, 47−54.
(31) Munro, M. Evaluated material properties for a sintered alpha-alumina. *J. Am. Ceram. Soc.* **1997**, *80*, 1919−1928.
(32) Krick, B. A.; Pitenis, A. A.; Harris, K. L.; Junk, C. P.; Sawyer, W. G.; Brown, S. C.; Rosenfeld, H. D.; Kasprzak, D. J.; Johnson, R. S.; Chan, C. D.; et al. Ultralow wear fluoropolymer composites: nanoscale functionality from microscale fillers. *Tribol. Int.* **2016**, *95*, 245−255.
(33) Bhattacharyya, S.; Behera, P. S. Synthesis and characterization of nano-sized α-alumina powder from kaolin by acid leaching process. *Appl. Clay Sci.* **2017**, *146*, 286−290.

(34) Maciver, D.; Tobin, H.; Barth, R. Catalytic aluminas I. Surface chemistry of eta and gamma alumina. *J. Catal.* **1963**, *2*, 485−497.
(35) Mangolini, L.; Thimsen, E.; Kortshagen, U. High-yield plasma synthesis of luminescent silicon nanocrystals. *Nano Lett.* **2005**, *5*, 655−659.
(36) Gresback, R.; Holman, Z.; Kortshagen, U. Nonthermal plasma synthesis of sizecontrolled, monodisperse, freestanding germanium nanocrystals. *Appl. Phys. Lett.* **2007**, *91*, 093119.
(37) Felbier, P.; Yang, J.; Theis, J.; Liptak, R. W.; Wagner, A.; Lorke, A.; Bacher, G.; Kortshagen, U. Highly luminescent ZnO quantum dots made in a nonthermal plasma. *Adv. Funct. Mater.* **2014**, *24*, 1988−1993.
(38) Greenberg, B. L.; Ganguly, S.; Held, J. T.; Kramer, N. J.; Mkhoyan, K. A.; Aydil, E. S.; Kortshagen, U. R. Nonequilibrium-plasma-synthesized ZnO nanocrystals with plasmon resonance tunable via Al doping and quantum confinement. *Nano Lett.* **2015**, *15*, 8162−8169.
(39) Thimsen, E.; Kortshagen, U. R.; Aydil, E. S. Nonthermal plasma synthesis of metal sulfide nanocrystals from metalorganic vapor and elemental sulfur. *J. Phys. D: Appl. Phys.* **2015**, *48*, 314004.
(40) Alvarez Barragan, A.; Ilawe, N. V.; Zhong, L.; Wong, B. M.; Mangolini, L. A nonthermal plasma route to plasmonic TiN nanoparticles. *J. Phys. Chem. C* **2017**, *121*, 2316−2322.
(41) Woodard, A.; Xu, L.; Barragan, A. A.; Nava, G.; Wong, B. M.; Mangolini, L. On the non-thermal plasma synthesis of nickel nanoparticles. *Plasma Process. Polym.* **2018**, *15*, 1700104.
(42) Holman, Z. C.; Kortshagen, U. R. A flexible method for depositing dense nanocrystal thin films: impaction of germanium nanocrystals. *Nanotechnology* **2010**, *21*, 335302.
(43) Firth, P.; Holman, Z. C. Aerosol impaction-driven assembly system for the production of uniform nanoparticle thin films with independently tunable thickness and porosity. *ACS Appl. Nano Mater.* **2018**, *1*, 4351−4357.
(44) Szymanski, S. F.; Seman, M. T.; Wolden, C. A. Effect of wall conditions on the self-limiting deposition of metal oxides by pulsed plasma-enhanced chemical vapor deposition. *J. Vac. Sci. Technol., A* **2007**, *25*, 1493−1499.
(45) Nguyen, H. M. T.; Tang, H.-Y.; Huang, W.-F.; Lin, M. C. Mechanisms for reactions of trimethylaluminum with molecular oxygen and water. *Comput. Theor. Chem.* **2014**, *1035*, 39−43.
(46) Tavakoli, A. H.; Maram, P. S.; Widgeon, S. J.; Rufner, J.; Van Benthem, K.; Ushakov, S.; Sen, S.; Navrotsky, A. Amorphous alumina nanoparticles: structure, surface energy, and thermodynamic phase stability. *J. Phys. Chem. C* **2013**, *117*, 17123−17130.
(47) Catherine, Y.; Talebian, A. Plasma deposition of aluminum oxide films. *J. Electron. Mater.* **1988**, *17*, 127−134.
(48) Kuech, T. F.; Veuhoff, E.; Kuan, T. S.; Deline, V.; Potemski, R. The influence of growth chemistry on the MOVPE growth of GaAs and $Al_xGa_{1-x}As$ layers and heterostructures. *J. Cryst. Growth* **1986**, *77*, 257−271.
(49) Kobayashi, N.; Makimoto, T. Reduced carbon contamination in OMVPE grown GaAs and AlGaAs. *Jpn. J. Appl. Phys.* **1985**, *24*, L824.
(50) Paparazzo, E. XPS analysis of iron aluminum oxide systems. *Appl. Surf. Sci.* **1986**, *25*, 1−12.
(51) Van den Brand, J.; Snijders, P. C.; Sloof, W. G.; Terryn, H.; De Wit, J. H. W. Acid- base characterization of aluminum oxide surfaces with XPS. *J. Phys. Chem. B* **2004**, *108*, 6017−6024.
(52) McCafferty, E.; Wightman, J. P. Determination of the concentration of surface hydroxyl groups on metal oxide films by a quantitative XPS method. *Surf. Interface Anal.* **1998**, *26*, 549−564.
(53) Van den Brand, J.; Sloof, W. G.; Terryn, H.; De Wit, J. H. W. Correlation between hydroxyl fraction and O/Al atomic ratio as determined from XPS spectra of aluminium oxide layers. *Surf. Interface Anal.* **2004**, *36*, 81−88.
(54) Zagrajczuk, B.; Dziadek, M.; Olejniczak, Z.; Sulikowski, B.; Cholewa-Kowalska, K.; Laczka, M. Structural investigation of gel-derived materials from the SiO_2−Al_2O_3 system. *J. Mol. Struct.* **2018**, *1167*, 23−32.
(55) Boumaza, A.; Favaro, L.; Lédion, J.; Sattonnay, G.; Brubach, J. B.; Berthet, P.; Huntz, A. M.; Roy, P.; Tétot, R. Transition alumina phases induced by heat treatment of boehmite: an X-ray diffraction and infrared spectroscopy study. *J. Solid State Chem.* **2009**, *182*, 1171−1176.
(56) Kortshagen, U.; Bhandarkar, U. Modeling of particulate coagulation in low pressure plasmas. *Phys. Rev. E: Stat. Phys., Plasmas, Fluids, Relat. Interdiscip. Top.* **1999**, *60*, 887.
(57) Liang, D. Generalized ellipsometry analysis of anisotropic nanoporous media: Polymer-infiltrated nanocolumnar and inverse-column polymeric films. Ph.D. Thesis, University of Nebraska, Lincoln, NE, 2015.
(58) Schmidt, D.; Schubert, E.; Schubert, M. Generalized ellipsometry determination of nonreciprocity in chiral silicon sculptured thin films. *Phys. Status Solidi A* **2008**, *205*, 748−751.
(59) Chang, P.-L.; Yen, F.-S.; Cheng, K.-C.; Wen, H.-L. Examinations on the critical and primary crystallite sizes during θ-to α-phase transformation of ultrafine alumina powders. *Nano Lett.* **2001**, *1*, 253−261.
(60) Sihvola, A. Mixing rules with complex dielectric coefficients. *Subsurf. Sens. Technol. Appl.* **2000**, *1*, 393−415.
(61) Voshchinnikov, N. V.; Videen, G.; Henning, T. Effective medium theories for irregular fluffy structures: aggregation of small particles. *Appl. Opt.* **2007**, *46*, 4065−4072.
(62) Pekonen, O.; Kärkkäinen, K.; Sihvola, A.; Nikoskinen, K. Numerical testing of dielectric mixing rules by FDTD method. *J. Electromagn. Waves Appl.* **1999**, *13*, 67−87.
(63) Wåckelgård, E. The experimental dielectric function of porous anodic alumina in the infrared region; a comparison with the Maxwell-Garnett model. *J. Phys.: Condens. Matter* **1996**, *8*, 4289.
(64) Markel, V. A. Introduction to the Maxwell Garnett approximation: tutorial. *J. Opt. Soc. Am. A* **2016**, *33*, 1244−1256.
(65) Wormeester, H.; Kooij, E. S.; Poelsema, B. Effective dielectric response of nanostructured layers. *Phys. Status Solidi A* **2008**, *205*, 756−763.
(66) Daugherty, J. E.; Graves, D. B. Particulate temperature in radio frequency glow discharges. *J. Vac. Sci. Technol., A* **1993**, *11*, 1126−1131.
(67) Mangolini, L.; Kortshagen, U. Selective nanoparticle heating: another form of nonequilibrium in dusty plasmas. *Phys. Rev. E: Stat., Nonlinear, Soft Matter Phys.* **2009**, *79*, 026405.
(68) McCallum, J. C.; Simpson, T. W.; Mitchell, I. V. Time resolved reflectivity measurements of the amorphous-to-gamma and gamma-to-alpha phase transitions in ion-implanted Al_2O_3. *Nucl. Instrum. Methods B* **1994**, *91*, 60−62.
(69) Simpson, T. W.; Wen, Q.; Yu, N.; Clarke, D. R. Kinetics of the amorphous→ γ→ α transformations in aluminum oxide: effect of crystallographic orientation. *J. Am. Ceram. Soc.* **1998**, *81*, 61−66.
(70) Eklund, P.; Sridharan, M.; Singh, G.; Bøttiger, J. Thermal Stability and Phase Transformations of γ-/Amorphous-Al_2O_3 Thin Films. *Plasma Process. Polym.* **2009**, *6*, S907−S911.
(71) Nakamura, R.; Shudo, T.; Hirata, A.; Ishimaru, M.; Nakajima, H. Nanovoid formation through the annealing of amorphous Al_2O_3 and WO_3 films. *Scr. Mater.* **2011**, *64*, 197−200.
(72) Nakamura, R.; Ishimaru, M.; Hirata, A.; Sato, K.; Tane, M.; Kimizuka, H.; Shudo, T.; Konno, T. J.; Nakajima, H. Enhancement of nanovoid formation in annealed amorphous Al_2O_3 including W. *J. Appl. Phys.* **2011**, *110*, 064324.
(73) Diouf, S.; Molinari, A. Densification mechanisms in spark plasma sintering: effect of particle size and pressure. *Powder Technol.* **2012**, *221*, 220−227.
(74) Kim, B.-C.; Lee, J.-H.; Kim, J.-J.; Ikegami, T. Rapid rate sintering of nanocrystalline indium tin oxide ceramics: particle size effect. *Mater. Lett.* **2002**, *52*, 114−119.

https://dx.doi.org/10.1021/acsomega.0c03353
ACS Omega 2020, 5, 24754−24761